Efficient charge separation and improved photocatalytic activity in Type-II & Type-III heterojunction based multiple interfaces in BiOCl$_{0.5}$Br$_{0.5}$-Q: DFT and Experimental Insight

Harshita Chawla [a], Seema Garg [a,*], Sumant Upadhyay [b], Jyoti Rohilla [c], Ákos Szamosvölgyi [d], Andras Sapi [d], Pravin Popinand Ingole [c], Suresh Sagadevan [e], Zoltán Kónya [d,f], Amrish Chandra [g,h]

[a] Department of Chemistry, Amity Institute of Applied Sciences, Amity University, Sector-125, Noida, 201313, Uttar Pradesh, India
[b] Department of Nanotechnology, Amity Institute of Nanotechnology, Amity University, Sector-125, Noida, 201313, Uttar Pradesh, India
[c] Department of Chemistry, Indian Institute of Technology, Delhi, Hauz Khas, New Delhi, 110016, India
[d] University of Szeged, Interdisciplinary Excellence Centre, Department of Applied and Environmental Chemistry, H-6720, Rerrich Béla tér 1, Szeged, Hungary
[e] Nanotechnology & Catalysis Research Centre, University of Malaya, Kuala Lumpur, 50603, Malaysia
[f] MTA-SZTE Reaction Kinetics and Surface Chemistry Research Group, Rerrich Béla tér 1, Szeged, H-6720, Hungary
[g] Amity Institute of Pharmacy, Amity University, Sector-125, Noida, 201313, Uttar Pradesh, India
[h] Amity Institute of Public Health, Amity University, Sector-125, Noida, 201313, Uttar Pradesh, India

HIGHLIGHTS

- The as fabricated BiOCl$_{0.5}$Br$_{0.5}$-Q exhibited nano-petal like structure.
- Simultaneous Type-III and type-II heterostructure were fabricated.
- The structural and functional relationship were investigated in detail.
- The First principle based DFT studies of heterostructures were carried out.
- 98% of Bisphenol A (Hazardous Material) was removed from contaminated water.

GRAPHICAL ABSTRACT
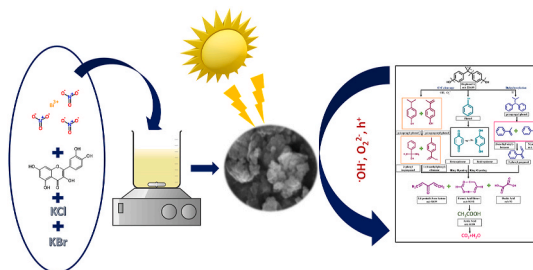
ARTICLE INFO

ABSTRACT

The nanostructured, inner-coupled Bismuth oxyhalides (BiOX$_{0.5}$X'$_{0.5}$; X, X' = Cl, Br, I; X≠X') heterostructures were prepared using Quercetin (Q) as a sensitizer. The present study revealed the tuning of the band properties of as-prepared catalysts. The catalysts were characterized using various characterization techniques for evaluating the superior photocatalytic efficiency and a better understanding of elemental interactions at interfaces formed

Abbreviations: BPA, Bisphenol A; Q, Quercetin; BiOBr, Bismuth oxybromide; BiOI, Bismuth Oxyiodide; BiOCl, Bismuth Oxychloride; MO, Methyl Orange; XPS, X-ray Photoelectron Spectroscopy;; BET, Brunauer-Emmett-Teller; BJH, Barrett-Joyner-Halenda; XRD, X-ray Diffraction; BE, Binding Energy; SEM, Scanning electron microscopy; TEM, Transmission Electron Microscopy; EDAX, Electron dispersive Assited X-Ray Spectroscopy; HR-TEM, High Resolution Transmission Electron Microscopy; SAED, Surface Assisted Electron Diffraction; JCPDS, Joint Committee on Powder Diffraction Standards; PEC, Photo-Electro-Chemical; Na-EDTA, Sodium Ethylene Diamine Tetrahydrate; IPA, Isopropyl Alcohol; BQZ, Benzoquinone; HPLC, High Profile Liquid Chromatography; LCMS, Liquid chromatography Mass Spectroscopy; TOC, Total Organic Carbon.

* Corresponding author.
E-mail address: sgarg2@amity.edu (S. Garg).

Bismuth oxychloride
Bismuth oxybromide
Interface formation
Quercetin invasion
Type-II heterojunction
Type-III heterojunction

in the heterojunction. The material ($BiOCl_{0.5}Br_{0.5}$-Q) reflected higher degradation of MO (about 99.85%) and BPA (98.34%) under visible light irradiation than $BiOCl_{0.5}I_{0.5}$-Q and $BiOBr_{0.5}I_{0.5}$-Q. A total of 90.45 percent of total organic carbon in BPA was removed after visible light irradiation on $BiOCl_{0.5}Br_{0.5}$-Q. The many-fold increase in activity is attributed to the formation of multiple interfaces between halides, conjugated π-electrons and multiple –OH groups of quercetin (Q). The boost in degradation efficiency can be attributed to the higher surface area, 2-D nanostructure, inhibited electron-hole recombination, and appropriate band-gap of the heterostructure. Photo-response of $BiOCl_{0.5}Br_{0.5}$-Q is higher compared to $BiOCl_{0.5}I_{0.5}$-Q and $BiOBr_{0.5}I_{0.5}$-Q, indicating better light absorption properties and charge separation efficiency in $BiOCl_{0.5}Br_{0.5}$-Q due to band edge position. First-principles Density Functional Theory (DFT) based calculations have also provided an insightful understanding of the interface formation, physical mechanism, and superior photocatalytic performance of $BiOCl_{0.5}Br_{0.5}$-Q heterostructure over other samples.

1. Introduction

Bisphenol A (BPA) is an important industrial chemical concomitant with polycarbonate plastics, epoxy resins, flame retardants, unsaturated polyester styrene, dental sealants, and lacquer coatings. BPA is reported as a typical endocrine-disrupting chemical. With a wide range of applications of BPA in industrial use, it is found in the water ecosystem. Its increasing concentration and bioaccumulation have elevated concerns towards human health. This leads to pathogenic disorders including endocrine disorders consisting of male and female infertility as it shows oestrogen-like and anti-androgen-like properties. This leads to substantial damage to tissues and organs, premature death of the foetus, prostate, breast cancer, etc. Because of its increasing day-to-day exposure, biomagnification is observed (Rochester, 2013a; Fenichel et al., 2013). Another pollutant of concern is methyl orange (MO), which is discharged from textile industries in very high concentrations to the main water stream. Various techniques including chemical and biological treatment were implemented for the decomposition of BPA and MO. But these techniques could not decompose it efficiently and completely. Visible-light-driven photocatalytic waste-water treatment, one of the physicochemical processes has shown efficient and cost-effective treatment in the removal of BPA and MO from effluent wastewater. Photocatalytic degradation is a non-toxic, low-cost, easy technique that has shown almost complete mineralization of BPA and MO into less toxic compounds (Rochester, 2013b; Garg et al., 2018a, 2018b)–(Rochester, 2013b; Garg et al., 2018a, 2018b).

To maximize the usage of solar energy and minimize cost and energy usage for waste-water treatment, there is a need of developing a highly efficient as well as highly stable photocatalyst that can acquire a wide wavelength range of solar light radiation. Over the past few decades, TiO_2 has been widely implemented as a photocatalyst for the degradation of recalcitrant pollutants. However, the limitation of TiO_2 due to its large band-gap has made it an inefficient catalyst to be implemented under photocatalyst (Noorjahan et al., 2004; Zhang et al., 2020; Réti et al., 2014; Salaeh et al., 2016; Jing et al., 2021). Therefore, bismuth-based catalysts have attracted researchers' concern due to their potential applications in photocatalytic environmental remediation. One such potential group includes bismuth oxyhalides that have been implemented by researchers for the removal of these recalcitrant pollutants. They exist in tetragonal matlockite structural form. BiOX is composed of [Bi_2O_2] slab interwoven with two halides (X = Cl, Br, and I) slabs forming layered structure along [110] plane. This leads to the development of electrostatic interaction between the slab layers. The electrostatic interaction helps in the better separation of photogenerated charge carriers, thereby imposing higher photocatalytic efficacy of the material (Tyagi et al., 2021; Sharma et al., 2019; Yadav et al., 2019a, 2019b; Garg et al., 2019)–(Tyagi et al., 2021; Sharma et al., 2019; Yadav et al., 2019a, 2019b; Garg et al., 2019).

The first principles DFT-based calculations were conducted for BiOX (X = Cl, Br, I) and indicated that valance band (VB) is present in hybridized form composed of 6p orbitals of Bi, np orbitals of halides and 2p orbitals of O, and conduction band (CB) comprises of 6s and 6p orbitals of Bi. The calculations have alluded that by altering the composition of

oxyhalides the band-gap can be tuned (Zhou et al., 2019; Wang et al., 2020). Therefore, the catalyst BiOX has been improvised using various techniques such as metal and non-metal doping, heterojunction formation, using sensitizers, etc. These approaches help in tuning band-gap, surface area, arrangement of layers, and size of the nanoparticles (Chawla et al., 2021; Etaiw and Marie, 2018; Gao et al., 2021; Zhao et al., 2020)–(Chawla et al., 2021; Etaiw and Marie, 2018; Gao et al., 2021; Zhao et al., 2020). Our research group has worked on modifying these bismuth oxyhalides using plant extract (*Azadirachta indica*) as a sensitizer and a great increase in efficiency was reported. Quercetin is a flavonoid constituent of plant extract which is majorly responsible for the higher separation of photogenerated charge carriers and is reported in our group's previous research work on BiOF(Yadav et al., 2019c, 2021; Garg et al., 2018c; Chawla et al., 2022)–(Yadav et al., 2019c, 2021; Garg et al., 2018c; Chawla et al., 2022).

Herein, we have implemented inner coupling between bismuth oxyhalides using quercetin as a sensitizer. A simple and facile hydrolysis method at 60 °C at neutral pH was used to fabricate $BiOX_{0.5}X'_{0.5}$ (X and X' = Cl, Br, I; and X≠X'). Therefore, as far as our approach optical and morphological properties as-fabricated catalysts have been modified (Sharma et al., 2019; Singh et al., 2018; Dutta et al., 2019; Lofrano et al., 2016; Chen et al., 2014; Huang et al., 2014; Jiang et al., 2015a; Ma et al., 2017)– (Sharma et al., 2019; Singh et al., 2018; Dutta et al., 2019; Lofrano et al., 2016; Chen et al., 2014; Huang et al., 2014; Jiang et al., 2015a; Ma et al., 2017). Due to the inclusion of quercetin in inner coupled oxyhalides, multiple interfaces were formed which increased the photocatalytic efficiency of the as-fabricated catalyst. Furthermore, a significant increment in photocatalytic degradation towards MO and BPA was observed. Based on the identified reaction intermediates, by-products (using HPLC and LCMS) (Hao, 2020; Li et al., 2014; Jiang et al., 2015b; Yu et al., 2015a; Sajid et al., 2018; Fu et al., 2018; Siao et al., 2018; Chen et al., 2018; Lee and Wang, 2019)–(Hao, 2020; Li et al., 2014; Jiang et al., 2015b; Yu et al., 2015a; Sajid et al., 2018; Fu et al., 2018; Siao et al., 2018; Chen et al., 2018; Lee and Wang, 2019), and reactive species (using quenching studies) (Chen et al., 2018; Lee and Wang, 2019; Li et al., 2020; Liu et al., 2020; Chou et al., 2021; Siao et al., 2019), the visible light photogenerated charge transfer mechanism between coupled oxyhalides and quercetin was inferred. Also, our DFT-based computational studies provided an insightful understanding and plausible mechanism for the improved photocatalytic activity in our samples.

2. Results and discussion

2.1. Structural and morphological analysis

The XRD patterns for as-fabricated photocatalysts ($BiOCl_{0.5}Br_{0.5}$-Q; $BiOCl_{0.5}I_{0.5}$-Q; $BiOBr_{0.5}I_{0.5}$-Q) are given in Fig. 1(a). The diffraction patterns of as-fabricated catalysts correspond to the pure phase of tetragonal bismuth oxychloride, bismuth oxybromide, and bismuth oxyiodide, well-matched with the Powder Diffraction File (PDF) no. JCPDS card no. 85–0861, JCPDS Card No. 73–2061 and JCPDS Card No. 73–2062 respectively [Joint Committee on Powder Diffraction

Standards (JCPDS)] (Xiao and Zhang, 2010; Wu et al., 2017; Deng et al., 2008) [Fig. S2(a)]. We have in our earlier studies conducted XRD for pristine BiOCl-G, BiOBr-G, and BiOI-G (Garg et al., 2018c, 2018d). Fig. 1 (a)(I) represented diffraction peaks of $BiOCl_{0.5}I_{0.5}$-Q with the strongest peak of diffraction at (110) plane with 2θ value of 32.15, with the growth of (102) plane with 2θ value of 33.51 indicating growth of nanoflower like structure. The diffraction pattern obtained for BiO-$Cl_{0.5}I_{0.5}$-Q corresponds with 2θ values at 24.75, 30.09, 32.15, 33.51, 46.14, 53.04, 56.16, 67.39, and 76.62 and were assigned to reflections from (011), (102) [BiOI], (110), (102) [BiOCl], (200), (211), (212), (220) and (310) hkl planes, respectively. Fig. 1(a)(II) represents diffraction peaks of $BiOCl_{0.5}Br_{0.5}$-Q with the strongest peak of diffraction corresponding to (110) plane at 2θ value 32.46. The growth of (001) pane at 2θ value 11.4 indicates the formation of nano-petals-like structures. Also, no trace of the (102) plane was obtained. The diffraction peaks for $BiOCl_{0.5}Br_{0.5}$-Q corresponds with 2θ values at 11.4, 22.9, 25.63, 32.46, 34.74, 40.10, 46.46, 48.28, 52.64, 53.90, 57.93, 68.11, 72.79 and 77.27 and were assigned to reflections from (001), (002), (011), (110), (003), (112), (200), (201), (104), (211), (203), (220), (301) and (310) hkl planes, respectively. Fig. 1(a)(III) represented the diffraction peaks of $BiOBr_{0.5}I_{0.5}$-Q with the strongest peak at (102) and (110) planes corresponding to 2θ value at 30.37 and 31.94 respectively indicating growth of nanoflower like structure. The diffraction peaks for $BiOBr_{0.5}I_{0.5}$-Q corresponds with 2θ values at 24.66, 30.37, 31.94, 33.71, 38.22, 45.79, 47.15, 52.95, 56.03, 66.99, and 76.05 and were assigned to reflections from (002), (102) [BiOI], (110), (102) [BiOBr], (112), (020), (113), (211), (212), (220), and (310) hkl planes, respectively.

Fig. 1(b) represents an expanded portion of XRD patterns of as-synthesized ($BiOCl_{0.5}Br_{0.5}$-Q; $BiOCl_{0.5}I_{0.5}$-Q; $BiOBr_{0.5}I_{0.5}$-Q) photocatalyst with 2θ range of 10–45° are represented for better comparison and a clear understanding of the changes in the unit cell dimensions due to the heterostructure formation between two oxyhalides and change in the structural arrangements. Nevertheless, the diffraction patterns confirm the incorporation of Cl & Br in $BiOCl_{0.5}Br_{0.5}$-Q; Cl & I in BiO-$Cl_{0.5}I_{0.5}$-Q; and Br & I in $BiOBr_{0.5}I_{0.5}$-Q. Importantly, no other diffraction peaks from pure Bismuth (Bi), Chlorine (Cl), Bromine (Br), Iodine(I), and Oxygen(O) chemical species were observed in the as-prepared sample. The obtained XRD does not represent any other peak of impurity thereby indicating uniform incorporation of quercetin in the composites. This approves the formation of requisite heterojunction. Additionally, the formed composites impart slightly wider FWHM due to the incorporation of quercetin, which indicates that the particle size of composite has decreased from parent semiconductors (Barik et al., 2021).

For analysing the functional groups in as fabricated samples, FTIR absorption spectra was conducted having spectral range from 400 to 4000 cm^{-1} [Fig. 1(c)]. In FTIR spectra of three composites, a wide range of absorption was observed from 2920 to 3687 cm^{-1} with maximum intensity at 3424 cm^{-1}. This broad range of absorption was accredited to

–OH groups of quercetin, while the peak at 2842 cm^{-1} was accredited to stretching of C–H of quercetin. A series of absorption peaks were observed at 1614 cm^{-1}, 1502 cm^{-1}, 1385 cm^{-1}, 1268 cm^{-1}, 1017.91 cm^{-1}, 809 cm^{-1}, and 664 cm^{-1} those were accredited to stretching of ketonic group (C=O), phenolic group (C_6H_5–OH) and ester linkage, asymmetric stretching of aromatic alkyl groups (ACH_3), and stretching of alkene groups (C=C), conquered due to presence of chromophores of quercetin (Catauro et al., 2015). The spectra represented another peak at 505 cm^{-1} due to the Bi–O group stretching in the tetragonal phase.

For analyzing morphological characteristics of as-fabricated BiO-$Cl_{0.5}Br_{0.5}$-Q, $BiOCl_{0.5}I_{0.5}$-Q, and $BiOBr_{0.5}I_{0.5}$-Q samples, FESEM, TEM, and HRTEM were conducted [Fig. 2(a–f)] and [Fig. 2(j–n)]. As represented in Fig. 2(a-b), quercetin-mediated synthesis of $BiOCl_{0.5}Br_{0.5}$-Q showed nanopetals like structures with two different size petals with an average size of 14 nm and 25 nm.

FESEM and EDAX were used to examine the morphological characteristics for the as-prepared samples of $BiOCl_{0.5}Br_{0.5}$-Q, $BiOCl_{0.5}I_{0.5}$-Q, and $BiOBr_{0.5}I_{0.5}$-Q as shown in Fig. 2(a-i). The quercetin-mediated synthesis of $BiOCl_{0.5}Br_{0.5}$-Q resulted in nano-petal-like structures with two different size petals with an average size of 14 nm and 25 nm, as shown in Fig. 2(a–b). Both nanopetals were widely dispersed with no aggregation, confirming the development of a composite. Interestingly, invading I with both Cl and Br separately leads to the accumulation of nanoplates of respective compounds in the form of 3-Dimensional hierarchical nanospheres. The size of $BiOCl_{0.5}I_{0.5}$-Q nanospheres ranged from 2 μm to 4 μm with two different size nanoplates with an average size of 11 nm and 44 nm. The size of $BiOBr_{0.5}I_{0.5}$-Q nanospheres ranged from 1 μm to 1.5 μm with different size nanoplates of 8 nm and 53 nm Fig. 2(c–f).

Fig. 2(j-n) represented TEM, SAED pattern, and HRTEM of as-fabricated $BiOCl_{0.5}Br_{0.5}$-Q photocatalyst, respectively. Analysis of Fig. 2(j) represented the particle size of nanoplates forming nano-petal structure is about 2.077 nm. The SAED (Selected Area Electron Diffraction) pattern reflected that nano-petals are polycrystalline in nature (Fig. 2k). The ring pattern thus formed by diffraction of electrons agreed with d-spacing of tetragonal phase bismuth oxychloride and bismuth oxybromide. The corresponding hkl values against d-spacing were assigned using JCPDS card no. 85–0861(BiOCl) and JCPDS Card No. 73–2061(BiOBr). Remarkably very low-intensity peaks were also identified thereby proving the purity of as-fabricated composite. The diffraction rings obtained in the SAED pattern correspond with planes having hkl values 202, 220, 310, and 313 for BiOCl, and 011, 110, 113, and 023 for BiOBr. Also, the obtained planes agreed with the XRD of the $BiOCl_{0.5}Br_{0.5}$-Q composite [Fig. 1(a)]. The Fig. 2(L) represents HRTEM, and two selected areas were zoomed in for calculating the d-spacing of fringes. The three different lattice fringes were observed. The selected yellow area reflected two types of fringes with d-spacing of 0.354 nm and 0.267 nm corresponding to (011) plane of BiOBr and (102) plane of BiOCl, respectively. The fringes obtained in selected pink
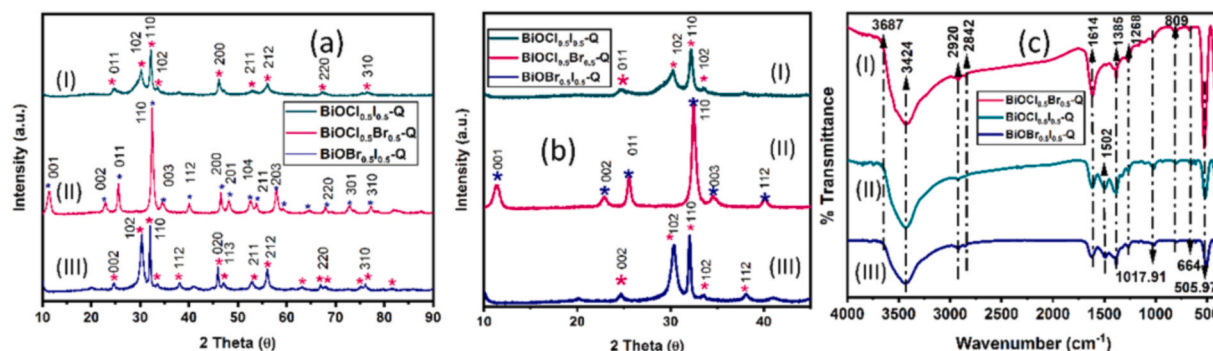

Fig. 1. (a, b) XRD Pattern and (c) FT-IR Analysis of $BiOCl_{0.5}I_{0.5}$-Q (green), $BiOCl_{0.5}Br_{0.5}$-Q (pink), and $BiOBr_{0.5}I_{0.5}$-Q (blue). (For interpretation of the references to colour in this figure legend, the reader is referred to the Web version of this article.)
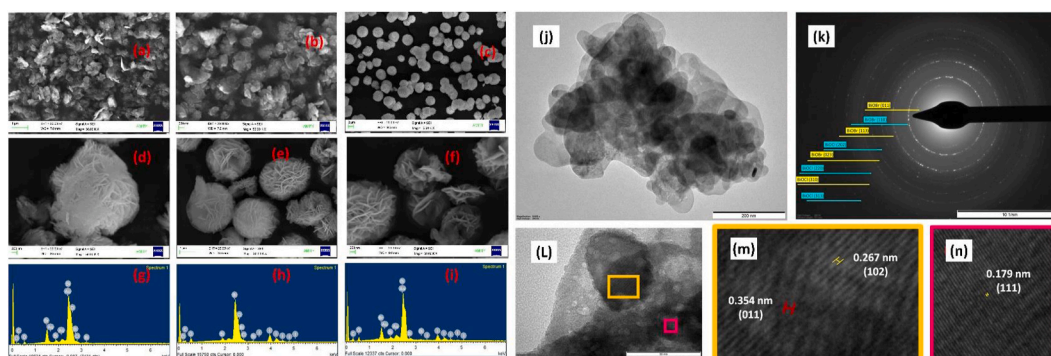
Fig. 2. SEM Images (a–b) $BiOCl_{0.5}Br_{0.5}$-Q, (c–d) $BiOCl_{0.5}I_{0.5}$-Q and (e–f) $BiOBr_{0.5}I_{0.5}$-Q; EDAX spectra of (g) $BiOCl_{0.5}Br_{0.5}$-Q, (h) $BiOCl_{0.5}I_{0.5}$-Q, and (i) $BiOBr_{0.5}I_{0.5}$-Q representing elemental composition of respective as-fabricated samples, (j) TEM image (k) SAED pattern with hkl values (L) HR-TEM (m) zoomed yellow part of L image and (n) zoomed pink part of L image of $BiOCl_{0.5}Br_{0.5}$-Q. (For interpretation of the references to colour in this figure legend, the reader is referred to the Web version of this article.)

area reflected d-spacing of 0.179 corresponding to (111) plane of Quercetin. This confirmed the presence of all three in fabricated composite (Lucida et al., 2016). TEM of $BiOCl_{0.5}I_{0.5}$-Q and $BiOBr_{0.5}I_{0.5}$-Q is represented in fig.S2(b& c) (S.I.).

The XPS spectra were used to analyse the electronic structures as well as the chemical composition of as-synthesized composites as shown in fig. S3 (a-f). The survey spectrum thus obtained showed expression of Bi, O, Br, Cl, C in $BiOCl_{0.5}Br_{0.5}$-Q; Bi, O, Cl, I, C in $BiOCl_{0.5}I_{0.5}$-Q; and Bi, O, Br, I, C in $BiOBr_{0.5}I_{0.5}$-Q as represented in fig. S3(a). Majorly, two binding energy peaks maxima at 165.07 eV and 159.7 eV were detected certifying to $Bi4f^{7/2}$ and $Bi4f^{5/2}$ which are main attributes of Bi^{3+}. Thus, obtained peaks correspond to Bi^{3+} of bismuth oxyhalides. The higher resolution spectra of O 1s displayed peak maxima at 530.3 eV, 532.0 eV, and 533.6 eV and were accredited to lattice oxygen, defective oxide &hydroxide, and organic oxygen respectively of bismuth oxyhalides [fig. S3(e)]. All high-resolution spectra were charge corrected to the aliphatic component of the C 1s spectra at 284.8eV, hydroxyl carbon and ether carbon at 286.03 eV, keto group at 287.6eV, and Carboxilla group at 288.7 eV [fig. S3(f)]. The peaks thus observed epitomize the presence of Quercetin in all as-prepared samples. Thus-obtained peaks for $Bi4f^{7/2}$, O1s, and C1s were nearly similar for all three fabricated samples. The high-resolution Cl2p spectra displayed peak maxima at 198.4 eV & 199.9 eV ($BiOCl_{0.5}Br_{0.5}$-Q) [fig. S3(c)] and 198.3 eV and 199.9 eV ($BiOCl_{0.5}I_{0.5}$-Q) [fig. S4(b) (S.I.)], were accredited to $Cl2p^{3/2}$ and $Cl2p^{1/2}$, respectively. Thus-obtained energy states validate the presence of monovalent chlorine. The high-resolution Br3d spectra represented two peculiar peak maxima at 68.8 eV & 69.8 eV ($BiOCl_{0.5}Br_{0.5}$-Q) [fig. S3(d)] and 68.7eV & 69.7eV ($BiOBr_{0.5}I_{0.5}$-Q) [fig. S5(b) (S.I.)] were accredited to $Br3d^{3/2}$ and $Br3d^{5/2}$, respectively. The spectra thus obtained for I represented peak maxima at 619.4 and 630.8 eV corresponds to $I 3d^{3/2}$ and $3d^{1/2}$ respectively [fig. S4(c) and fig. S5(c) (S.I.)].

The specific surface area and pore size of synthesized **$BiOCl_{0.5}Br_{0.5}$-Q, $BiOCl_{0.5}I_{0.5}$-Q, and $BiOBr_{0.5}I_{0.5}$-Q** were measured using Brunauer–Emmett–Teller (BET) N_2 adsorption-desorption isotherm at a relative pressure ($P/P_0 = 0$–0.99) and BJH pore size analyser. According to IUPAC nomenclature of isotherm classification $BiOCl_{0.5}Br_{0.5}$-Q, $BiOCl_{0.5}I_{0.5}$-Q, and $BiOBr_{0.5}I_{0.5}$-Q followed Type-IV Isotherm, with H-4, and H-5 hysteresis loop, respectively [fig.S6(b-d), tableS.1(S.I.)]. The surface area thus obtained for $BiOCl_{0.5}Br_{0.5}$-Q, $BiOCl_{0.5}I_{0.5}$-Q, and $BiOBr_{0.5}I_{0.5}$-Q was 28.68m^2g^{-1}, 23.17m^2g^{-1}, 21.951m^2g^{-1}, respectively. The increased surface area of $BiOCl_{0.5}Br_{0.5}$-Q is due to an increase in surface porosity and roughness of composite which increased adsorption capacity thereby inducing the highest photocatalytic degradation efficiency of the catalyst. The reason behind an increase in degradation efficiency is higher absorption of visible light radiation and thereby more active species are generated and boosting the interaction of pollutants and reactive species. The measured pore size was 15.20 nm, 14.39 nm, and

12.57 nm for $BiOCl_{0.5}Br_{0.5}$-Q, $BiOCl_{0.5}I_{0.5}$-Q, and $BiOBr_{0.5}I_{0.5}$-Q, respectively. The average BJH pore volume was 48.7$cm^3g^{-1}$for $BiOCl_{0.5}Br_{0.5}$-Q, and 46.9cm^3g^{-1} for both $BiOCl_{0.5}I_{0.5}$-Q, and $BiOCl_{0.5}I_{0.5}$-Q. The higher BET and mesoporosity of $BiOCl_{0.5}Br_{0.5}$-Q are helpful in better adsorption of pollutant on catalyst surface further leading to favourable enhancement of photocatalytic and photo-electrochemical activity.

2.2. Optical analysis

UV–Vis diffuse absorption spectra (UV–vis. DRS) was recorded to analyse the optical properties of as-fabricated quercetin-mediated $BiOCl_{0.5}Br_{0.5}$-Q, $BiOCl_{0.5}I_{0.5}$-Q, and $BiOBr_{0.5}I_{0.5}$-Q. Fig.S6(a) depicts the Tauc plot, which was used to determine the bandgap of as-fabricated samples. The wavelength absorption edges reflected that the material absorbs light in the visible region (i.e., above 400 nm). The plot signifies that composite $BiOCl_{0.5}Br_{0.5}$-Q absorbs light at a lower wavelength than $BiOCl_{0.5}I_{0.5}$-Q, and $BiOBr_{0.5}I_{0.5}$-Q in the visible region of 400–700 nm. The Eg values of $BiOCl_{0.5}Br_{0.5}$-Q, $BiOCl_{0.5}I_{0.5}$-Q, and $BiOBr_{0.5}I_{0.5}$-Q are 2.40 eV, 2.13 eV, and 2.14 eV, respectively. The relatively higher bandgap of $BiOCl_{0.5}Br_{0.5}$-Q than the other two as fabricated catalyst lowers the recombination rate of photogenerated charge carriers further enhancing photocatalytic efficiency of $BiOCl_{0.5}Br_{0.5}$-Q.

2.3. Computational analysis

The structural parameters calculated for bulk BiOX (X = Cl, Br) a = 7.82 Å, c = 7.87 Å are in good agreement with other reports (Zhang et al., 2017; Tang et al., 2016), which ensures our reasonable computational results. The calculated electronic band structures and projected density of states are shown in fig.S7(a-e) and fig.S8(a-e) respectively. The calculated indirect band-gap values for BiOCl, BiOBr, $BiOCl_{0.5}Br_{0.5}$, $BiOCl_{0.5}I_{0.5}$, and $BiOBr_{0.5}I_{0.5}$ are 2.14, 1.97, 1.95, 1.46, and 1.94 eV, respectively. The small band-gap is attributed to the well-known underestimation of GGA (genralised gradient approximation), however, in the present study, we are more interested to know the bandgap changes through doping, rather than in calculating the absolute values. The decreased band gap was observed because of the strong electronegativity of Cl and the lower energy level of Cl compared to that of Br and I. The trend observed in the changes in bandgap corroborated well with our experimental results. As shown in fig.S7, the $BiOCl_{0.5}Br_{0.5}$ structure has more dispersed valence and conduction bands than other structures, which is beneficial to the fast mobility of photogenerated charge carriers, resulting in improved photocatalytic performance. For BiOI electronic band structure and PDOS is represented in fig.S6 & S7(S.I.) respectively.

As shown in fig.S8(S.I.), the Bi 6p states dominate the conduction band region and have the least contribution to the valence band in each

structure. The contribution of X (=Cl, Br, I) 2p orbitals is seen negligible in the conduction band, and prominent in the valence band region. Therefore, these species may be assigned to the p-to-p charge transfer type, like the descriptions for the p-to-d charge transfer type for transition metal compounds. The charge transfer energy might decrease with the reduction of electronegativity in species (Chawla et al., 2021; Huang, 2009).

2.4. Photocatalytic performance of as fabricated composites

The annexation of modifying and tuning of band energy as-fabricated inner coupled bismuth oxyhalides (BiOCl$_{0.5}$Br$_{0.5}$-Q, BiOCl$_{0.5}$I$_{0.5}$-Q, & BiOBr$_{0.5}$I$_{0.5}$-Q) using quercetin as sensitizer were deliberated by degrading Methyl Orange (MO, 20 ppm) dye and Bisphenol A (BPA, 30 ppm) under visible light irradiation. The photocatalytic activity of a fabricated BiOCl–N catalyst was chosen as a reference for understanding the role of developed heterojunction between two oxyhalides. In the lack of photocatalyst, no degradation was observed in the case of both MO and BPA. The effect of photocatalysis was studied by varying concentrations of BPA, pH of the solution, and catalyst concentration. The detailed experiments are listed below.

2.4.1. Effect of inner coupling between oxyhalides

To examine the effect of inner-coupling of halides, the photocatalytic activity of as-prepared samples was carried out using selected pollutant slurry. As photocatalysis is directly associated with the surface of the catalyst, adsorption of respective pollutants plays a major role in the further fragmentation process of pollutants. The adsorption-desorption property of MO dye on fabricated bismuth oxyhalides samples was carried out in the absence of light till equilibrium was obtained. The stability was obtained after 60 min. Out of all, three fabricated inner coupled oxyhalides, BiOCl$_{0.5}$Br$_{0.5}$-Q showed about 70% adsorption within 60 min, and it was approximately 30% for BiOCl$_{0.5}$I$_{0.5}$-Q and BiOBr$_{0.5}$I$_{0.5}$-Q both. This is mainly due to the higher surface area of BiOCl$_{0.5}$Br$_{0.5}$-Q over as-fabricated BiOCl$_{0.5}$I$_{0.5}$-Q and BiOBr$_{0.5}$I$_{0.5}$-Q. Upon irradiation of visible light, 99.85% degradation of MO was obtained for BiOCl$_{0.5}$Br$_{0.5}$-Q and nearly 87.15 & 87.05 for BiOCl$_{0.5}$I$_{0.5}$-Q and BiOBr$_{0.5}$I$_{0.5}$-Q respectively [fig.S9.(a)(S.I.)]. Similarly, for BPA, about 1.02%, 0.71%, and 0.95% adsorption in dark were obtained using BiOCl$_{0.5}$Br$_{0.5}$-Q, BiOCl$_{0.5}$I$_{0.5}$-Q, and BiOBr$_{0.5}$I$_{0.5}$-Q, respectively. On exposure to the visible light source, a maximum of 98.41%, 80.449%, and 81.82% degradation of 30 ppm BPA was obtained using BiOCl$_{0.5}$Br$_{0.5}$-Q, BiOCl$_{0.5}$I$_{0.5}$-Q, and BiOBr$_{0.5}$I$_{0.5}$-Q respectively within 19 h [Fig. 3(a)]. The highest adsorption and degradation activity was obtained for BiOCl$_{0.5}$Br$_{0.5}$-Q. In our previously reported work, a maximum of 78.81% of 20 ppm BPA was degraded using BiOCl–N (Garg et al.,

2018d). This showed that coupling bromide has increased the photoactivity of as-fabricated catalysts to a great extent. The incorporation of Quercetin in the fabricated samples has boosted the optical window for harvesting photogenerated charge carriers and hindered recombination for a longer interval of time.

Further using Langmuir-Hinshelwood models, the photocatalytic graphs were fitted and rate constants for as-fabricated samples were determined. This showed that both MO and BPA degradation follow pseudo-first-order kinetics. BiOCl$_{0.5}$Br$_{0.5}$-Q exhibited the highest rate constants with 0.06514 (min^{-1}) and 0.003312 (min^{-1}) for MO [fig.S9 (d)(S.I.)] and BPA respectively which was about 2 & 2.5 times higher than the other two fabricated samples respectively [Fig. 3(b)]. The R^2 value was also calculated that reflected that data is highly correlated.

2.4.2. Effect of pH and concentration of pollutant slurry

Even though the concentration of dye effluents observed in the main water stream is in the range of ng/L-mg/L, it is very high in industrial effluent. So, the concentration of MO dye was varied from 10 mg/L to 40 mg/L. When the concentration of MO dye was only 10 mg/L, complete photocatalytic degradation took place within 60 min but increasing concentration to 20 mg/L took 80 min for complete degradation and increasing concentration to 40 mg/L, 82% degradation was observed within 80 min. This represented that with increasing concentration of dye, the degradation efficiency decreased, and the time required for its abolition increased. The pseudo-first-order kinetics was observed [Fig. S9(b, e)(S.I.)]. This concluded that at lower concentrations of MO dye, the active sites present on catalysts surface were adequate to bear the load of dye molecules, and at higher concentrations, the active sites of catalysts in comparison with concentration of pollutant are lower and thus the availability of photogenerated charge carriers also decreases. The rate of reaction, thus observed for a lower concentration of MO dye was comparatively higher, accordingly higher degradation efficiency in less time interval was observed.

To scrutinize the optimum pH for maximizing the degradation efficiency of pollutants, degradation experiments were carried out in acidic (pH = 2), neutral (pH = 7), and basic (pH = 11) environments. When the pH of MO slurry was acidic, both dye solution and catalyst became positively charged and very few hydroxyl ions were generated. This highly reduces the adsorption of MO on the BiOCl$_{0.5}$Br$_{0.5}$-Q surface. Also, due to less availability of hydroxyl ions in slurry, only 37% degradation for 20 ppm MO was observed in an acidic environment. When the pH of MO slurry was neutral, complete removal was observed in 80 min. The pseudo-first-order kinetics was observed [Fig. S.9(c, f)(S.I.)]. As the pH of the slurry was turned basic, the availability of active species increased, and complete degradation was observed within 60 min of visible light irradiation. But in the case of BPA, maximum
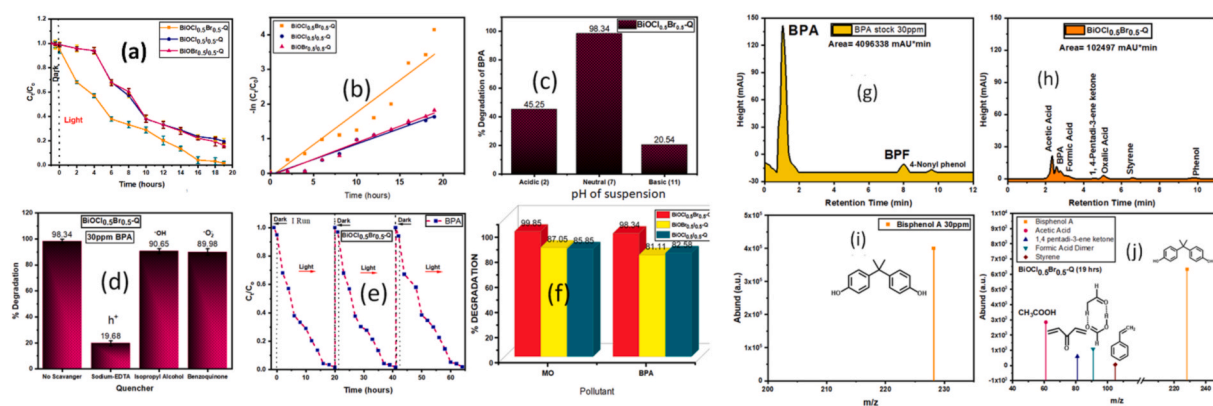

Fig. 3. (a) Degradation of 30 ppm BPA in visible light, (b) kinetic linear stimulation representing pseudo-first-order reaction, (c) 30 ppm BPA degradation with change in pH, (d) radical Quenching studies for BPA degradation, (e) repetition studies of BPA degradation, (f) comparison of percentage degradation of MO and BPA using coupled oxyhalides; HPLC of **(g)**30 ppm BPA stock solution and, **(h)** degraded BPA solution using BiOCl$_{0.5}$Br$_{0.5}$-Q; LCMS of (i) 30 ppm BPA, (j) BPA degraded into less toxic organic compounds.

degradation was observed at neutral pH [Fig. 3(c)]. This may be due to the generation of repulsive forces between catalysts and pollutants in both acidic and basic pH conditions. Also, a higher repulsion was observed in basic pH. Similar reports have been published with the degradation of colourless recalcitrant pollutants which reflected the repulsive forces between molecules in basic pH (Sekar et al., 2021; Li et al., 2021a, 2021b; Wu et al., 2020)–(Sekar et al., 2021; Li et al., 2021a, 2021b; Wu et al., 2020).

2.4.3. Effect of quenching radicals

For investigating the role of photogenerated active species, radical quenching studies were carried out on $BiOCl_{0.5}Br_{0.5}$-Q (Jiang et al., 2015c; Yu et al., 2015b; Xiao et al., 2014). Firstly, 20 ppm MO slurry was taken and Sodium-EDTA, Isopropanol (IPA), and Benzoquinone (BQZ) were chosen for trapping holes (h^+), hydroxyl radical (·OH), and superoxide radical (·O^{2-}) respectively. When results were compared with a slurry solution containing no scavenger, fragmentation efficacy of MO was remarkably declined in presence of respective scavengers. This reflected that all three radicals played a crucial role in the photocatalytic disintegration of MO and holes were highly responsible for the degradation of MO [Fig.S9(g)(S.I.)]. In the case of BPA, a similar investigation was carried out using $BiOCl_{0.5}Br_{0.5}$-Q. The studies reflected that a slurry containing IPA and BQZ showed very less inhibition in photocatalytic performance when compared with the results of a slurry solution containing no scavenger. On the contrary, extricate inhibition was detected in a slurry containing sodium EDTA. This concluded that h^+ is majorly responsible for the degradation of BPA and ·OH, and ·O^{2-} are very less effective in the degradation of BPA [Fig. 3(d)]. Also, to determine the stability of as-fabricated $BiOCl_{0.5}Br_{0.5}$-Q, the sample was washed and reused for three consecutive runs and the degradation thus obtained was nearly similar [Fig. 3(e)]. A comparative degradation of MO and BPA using as-fabricated samples is represented in Fig. 3(f). The photocatalytic results thus obtained for MO and BPA degradation with their rate constants are summarized in table S2 and a comparative study with earlier reported catalyst is summarized in table S3(S.I.).

2.4.4. Determining reaction intermediates and degradation mechanism

For identification of possible formed intermediates during photocatalytic degradation process of BPA over as-fabricated $BiOCl_{0.5}Br_{0.5}$-Q [Fig. 3(g-j)], $BiOCl_{0.5}Br_{0.5}$-Q and $BiOBr_{0.5}I_{0.5}$-Q [Fig.S10 (S.I.)], HPLC and LCMS analysis were conducted. In the photocatalytic degradation system, majorly five organic compounds were identified as styrene (m/z=104), 1,4-pentadi-3-ene ketone ($m/z = 80.99$), formic acid dimer (m/z=90.93), oxalic acid (m/z=90), and acetic acid (m/z=61.08) with trace of phenol (m/z=93). Based on the results thus obtained above, the degradation pathway of BPA was designed. The BPA degradation followed two pathways (a) C–C cleavage in which hydroxyl and superoxide radicals play a major role, and (b) dehydroxylation which occurs majorly in presence of holes [Fig. 11(S.I.)] (Lee and Wang, 2019; Chou et al., 2021). In the degraded reaction mixture, either phenol, p-benzoquinone, p-isopropyl phenol, p-isopropenyl phenol, 2-phenyl isopropanol, and 1-(4-methyl phenyl) ethenone were not identified. It reflected that either the complete conversion of these aromatic compounds took place, or the degradation pathway could be through dehydroxylation. Detection of a small amount of styrene confirmed the degradation pathway of BPA. Earlier, radical quenching studies have also confirmed the crucial role of h^+ in the disintegration of BPA instead of ·OH and ·O^{2-} radicals. Also, after 19 hrs of visible light irradiation, TOC (total organic carbon) was assayed. The studies reflected removal of 90.45%, 78.71%, and 80.45% TOC in BPA using $BiOCl_{0.5}Br_{0.5}$-Q, $BiOCl_{0.5}I_{0.5}$-Q, and $BiOBr_{0.5}I_{0.5}$-Q, respectively.

2.5. Photo-electrochemical mechanism

The competence of separation and transportation of photogenerated charges encircles an important role in the determination of

photocatalytic efficiency of as-fabricated samples, which can be pondered using PEC (photo-electrochemical) properties. The plot is in Fig. 4(a), represents the transient photocurrent density of samples with illumination ON/OFF conditions at 1.23 V vs RHE. The plot indicated that as-fabricated $BiOCl_{0.5}Br_{0.5}$-Q is comparatively more stable under ON and OFF light conditions in comparison with $BiOCl_{0.5}I_{0.5}$-Q and $BiOBr_{0.5}I_{0.5}$-Q. Photo-response of coupled $BiOCl_{0.5}Br_{0.5}$-Q is comparatively higher than $BiOCl_{0.5}I_{0.5}$-Q and $BiOBr_{0.5}I_{0.5}$-Q, indicating that coupling of (Cl, Br) has enhanced light absorption properties and charge separation efficiency in comparison with (Cl, I) & (Br, I) due to their band edge position. As represented, the photocurrent response of $BiOCl_{0.5}I_{0.5}$-Q was higher than $BiOBr_{0.5}I_{0.5}$-Q till 250s but after that photocurrent response of $BiOBr_{0.5}I_{0.5}$-Q was enhanced. This represents an increase in photocurrent stability of material with an increase in exposure time. Also, it indicated that the photocurrent density of $BiOCl_{0.5}Br_{0.5}$-Q is consistent with the time interval, indicating higher stability of the as-fabricated catalyst. But for $BiOCl_{0.5}I_{0.5}$-Q, stability decreases with the increase in a time interval. Similar results were obtained during photocatalytic experiments [Fig. 3(a)].

Further, for studying charge transfer efficiency at the formed interface of material photoelectrodes, Electrochemical impedance spectroscopy (EIS) was employed. Nyquist plot as represented in Fig. 4(b) was acquired in dark at 1.23V vs. RHE. The three curves thus obtained for $BiOCl_{0.5}Br_{0.5}$-Q, $BiOCl_{0.5}I_{0.5}$-Q, and $BiOBr_{0.5}I_{0.5}$-Q have different radii. The curvature radii thus obtained in the Nyquist plot relates to charge transfer resistance at electrode/electrolyte interface. The semicircle for $BiOCl_{0.5}Br_{0.5}$-Q is comparatively smaller followed by $BiOCl_{0.5}I_{0.5}$-Q and lastly $BiOBr_{0.5}I_{0.5}$-Q, thereby indicating $BiOCl_{0.5}Br_{0.5}$-Q has more facile charge transfer kinetics in comparison with the other two fabricated samples. This indicated promotion of water oxidation reaction and higher cathodic shift in onset potential of $BiOCl_{0.5}Br_{0.5}$-Q. Therefore, the factor that can be accountable for the higher photocatalytic response of as-fabricated $BiOCl_{0.5}Br_{0.5}$-Q is a higher bandgap in comparison with $BiOCl_{0.5}I_{0.5}$-Q and $BiOBr_{0.5}I_{0.5}$-Q, which has decreased recombination of photogenerated charge carriers. Fig. 4(c) represented current density data with respect to an applied bias voltage. The dotted lines represent current density in absence of light and solid lines represent current density in presence of light for as-fabricated samples. The maximum photocurrent density is obtained for $BiOCl_{0.5}Br_{0.5}$-Q (2.06 mA/cm^2) followed by $BiOBr_{0.5}I_{0.5}$-Q (0.93 mA/cm^2) and $BiOCl_{0.5}I_{0.5}$-Q (0.63 mA/cm^2) 2V vs RHE. This indicated that maximum interfacial charge transfer took place in $BiOCl_{0.5}Br_{0.5}$-Q. Thus, it concluded that the light absorption range has also increased, thereby increasing the internal separation of photogenerated charge carriers, and thereby reducing the barrier in charge transfer. Based on the aforementioned XRD, FT-IR, SEM, XPS, UV-DRS, photocatalytic experiments, radical quenching experiments, HPLC, and LCMS analysis, a feasible visible light spectrum has driven type-III and type-II heterostructure photogenerated charge transfer mechanism for $BiOCl_{0.5}Br_{0.5}$-Q system was performed and shown in Fig. 4(c). Under visible light irradiation, Quercetin, BiOCl, and BiOBr are photoexcited and generate electron-hole pairs. Quercetin CB and VB potential are −5.27 eV and −3.86 eV determined using cyclic voltammetry technique. As quercetin molecule absorbs visible light radiations, photogenerated charge species including electrons and holes are localized in CB and VB, respectively. Due to the difference in Fermi levels in CB potential, electrons are transferred from CB of Quercetin to CB of BiOBr. The junction formed is a broken gap, type-III heterojunction. Owing to different work functions, there is a development of electrostatic interactions that is constructive for the separation of photogenerated charge carriers. Due to the difference in Fermi energy levels of BiOBr and BiOCl, the interfacial electron transfer from CB of BiOBr to CB of BiOCl takes place and holes are transferred from VB of BiOCl to VB of BiOBr. This leads to downward and upward band bending of CB and VB in the direction of interface, respectively. This forms a conventional type-II charge transfer mechanism and thereby retaining holes as well as electrons with stronger oxidation and reduction ability. The
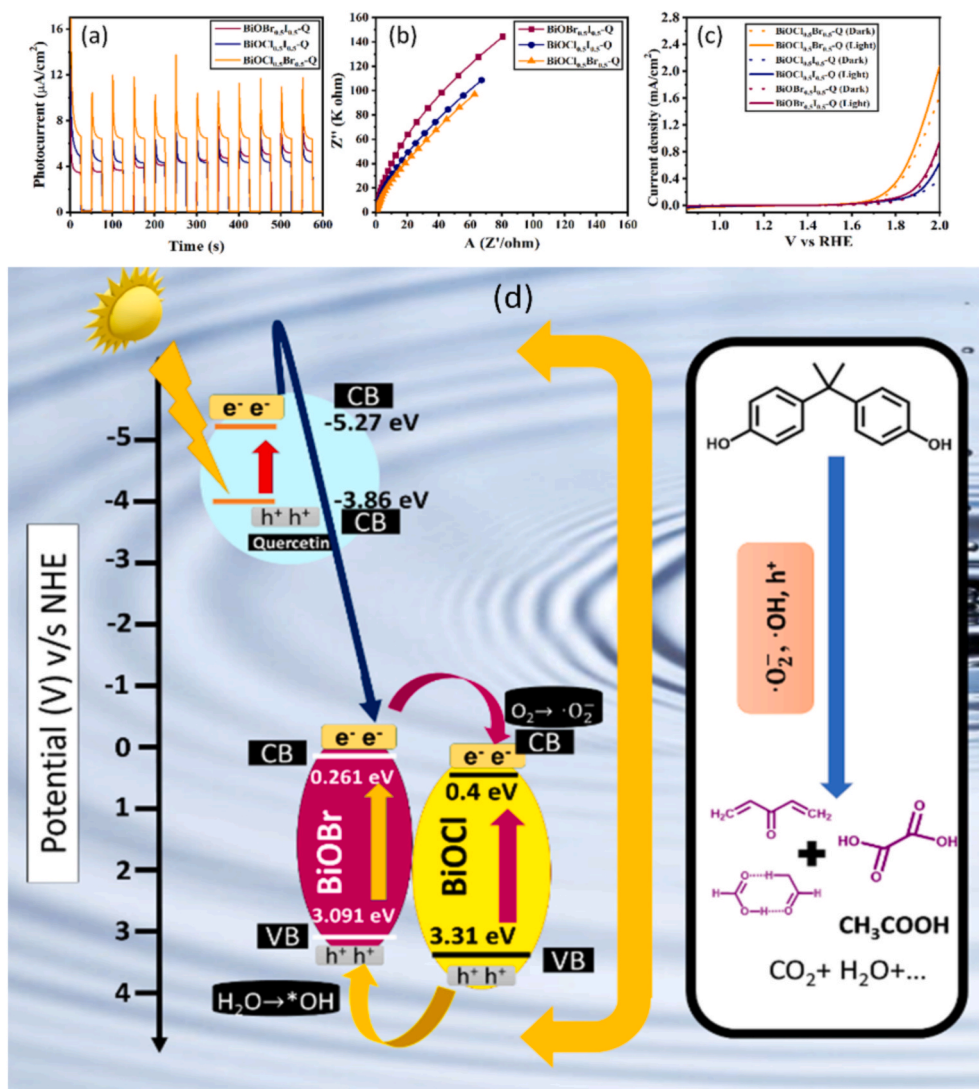
Fig. 4. (a) Photocurrent response, (b) EIS, and (c) current density [J] v/s bias voltage [V v/s RHE] for $BiOCl_{0.5}Br_{0.5}$-Q (orange), $BiOCl_{0.5}I_{0.5}$-Q (blue) and $BiOBr_{0.5}I_{0.5}$-Q (violet) (d) Mechanism of charge transfer between interfaces leading to the generation of reactive species and degradation of bisphenol A to smaller organic molecules. (For interpretation of the references to colour in this figure legend, the reader is referred to the Web version of this article.)

photogenerated electrons and holes are capable of producing $\cdot O^{2-}$ by reacting with atmospheric oxygen and hydroxyl free radicals by oxidizing H_2O molecules, respectively. Alongside, a part of holes can directly oxidize BPA into smaller organic molecules. Also, the amount of pollutant adsorbed on the surface of the catalyst directly affects the percentage and the rate of degradation of the pollutant. Therefore, in contrast with type-II heterojunction, a combination of type-III and type-II heterojunctions were formed, that retains the photogenerated electrons and holes with stronger reduction and oxidation ability for a longer duration. Based on the above inference, the photocatalyst BiO-$Cl_{0.5}Br_{0.5}$-Q has shown improved photocatalytic activity in visible light irradiation and it can be attributed to the transfer of photogenerated charge carriers between multiple interfaces and alteration in-band structure (Li et al., 2021c; Choi et al., 2021).

3. Conclusions

The present study has established the development of effective type-III and type-II heterojunction between Quercetin & BiOBr, and BiOBr & BiOCl, respectively. The as-fabricated photocatalyst $BiOCl_{0.5}Br_{0.5}$-Q is highly efficient in the degradation of an azo dye (MO), and recalcitrant organic pollutant (BPA) with maximum efficiency of 99.85% and

98.34% respectively in an aqueous medium under visible light irradiation in comparison with $BiOCl_{0.5}I_{0.5}$-Q and $BiOBr_{0.5}I_{0.5}$-Q. The characterizations revealed the 2D-nanopetals-like structure and higher surface area of $BiOCl_{0.5}Br_{0.5}$-Q, thereby increasing adsorption and degradation of pollutant on the surface of the catalyst. Electrochemical studies reflected higher as well as stable photocurrent response, with maximum and facile interfacial charge transfer in $BiOCl_{0.5}Br_{0.5}$-Q in comparison with $BiOCl_{0.5}I_{0.5}$-Q and $BiOBr_{0.5}I_{0.5}$-Q. The intermediates were recognized using HPLC and LCMS and it was revealed that catalyst mainly followed the dehydroxylation pathway and later, it was confirmed using radical quenching studies. The increase in photocatalytic activity was accredited to a suitable band edge position in $BiOCl_{0.5}Br_{0.5}$-Q that inhibits electron-hole recombination and thereby provides adequate active sites for photodegradation of pollutants. Our first-principles DFT calculation revealed the well-separation of charge carriers, resulting in a low carrier's recombination and type-II band alignment, which favors the enhanced photocatalytic activity in $BiOCl_{0.5}Br_{0.5}$ heterostructure. Our theoretical and experimental results provide a comprehensive investigation of $BiOX_{0.5}X'_{0.5}$ (X, X' = Cl, Br, I; X≠X') heterostructure, which would provide a useful strategy for further optimizing the photocatalytic performance of heterojunction and its future applications.

Author contribution statement

Conceptualization & Supervision, S.G., S.U., A.C., A.S., S.S., Z.K., and P.P.I.; Methodology, S.G., H.C., J.R., S.U.; Validation, S.G., S.U., A.C., S.S., Z.K., A.S., and P.P.I.; Formal Analysis, H.C., S.G., A.K., S.U., J.R., and A.S..; Funding acquisition S.G., A.S., S.U., Z.K., and P.P.I.; Investigation, H.C., S.G., A.K., J.R., and S.U.; Project administration S.G., and A.C.; Resources, S.G., S.U., Z.K., A.C., and P.P.I.; Software H.C., S.U., J.R., and A.K.; Data Curation, S.G., S.U., A.S., S.S., Z.K., and P.P.I.; Writing-Original Draft Preparation, H.C., S.U., S.G., and J.R.; Writing-Review & Editing, S.U., S.G., A.C., A.S., S.S., Z.K., and P.P.I.; Visualization, S.G. and H.C.

Declaration of competing interest

The authors declare that they have no known competing financial interests or personal relationships that could have appeared to influence the work reported in this paper.

Acknowledgments

Appendix A. Supplementary data

Supplementary data to this article can be found online at https://doi.org/10.1016/j.chemosphere.2022.134122.

References

Barik, R., Kumar Yadav, A., Nath Jha, S., Bhattacharyya, D., Ingole, P., P, 2021. Two-dimensional tungsten oxide/selenium nanocomposite fabricated for flexible supercapacitors with higher operational voltage and their charge storage mechanism. ACS Appl. Mater. Interfaces 13, 8102–8119. https://doi.org/10.1021/acsami.0c15818.

Catauro, M., Papale, F., Bollino, F., Piccolella, S., Marciano, S., Nocera, P., Pacifico, S., 2015. Silica/quercetin sol–gel hybrids as antioxidant dental implant materials. https://doi.org/10.1088/1468-6996/16/3/035001. http://www.tandfonline.com/action/journalInformation?show=aimsScope&journalCode=tsta20#.VmBmuzZFCUk.16.

Chawla, H., Chandra, A., Ingole, P.P., Garg, S., 2021. Recent Advancements in Enhancement of Photocatalytic Activity Using Bismuth-Based Metal Oxides Bi2MO6 (M=W, Mo, Cr) for Environmental Remediation and Clean Energy Production.

Chawla, H., Garg, S., Ingole, P.P., Chandra, A., 2022. Immobilization of Photocatalytic Material on the Suitable Substrate, pp. 445–473. https://doi.org/10.1007/978-3-030-77371-7_15.

Chen, H.L., Lee, W.W., Chung, W.H., Lin, H.P., Chen, Y.J., Jiang, Y.R., Lin, W.Y., Chen, C. C., 2014. Controlled hydrothermal synthesis of bismuth oxybromides and their photocatalytic properties. J. Taiwan Inst. Chem. Eng. 45, 1892–1909. https://doi.org/10.1016/J.JTICE.2013.12.015.

Chawla, Harshita, Saha, Meghna, Upadhyay, Sumant, Rohilla, Jyoti, Ingole, Pravin Popinand, Sapi, Andras, Szenti, Imre, et al., 2021. Enhanced photocatalytic activity and easy recovery of visible light active MoSe 2/BiVO 4 heterojunction immobilized on Luffa cylindrica–experimental and DFT study. Environ. Sci.: Nano 8 (10), 3028–3041.

Chen, C.C., Fu, J.Y., Chang, J.L., Huang, S.T., Yeh, T.W., Hung, J.T., Huang, P.H., Liu, F. Y., Chen, L.W., 2018. Bismuth oxyfluoride/bismuth oxyiodide nanocomposites enhance visible-light-driven photocatalytic activity. J. Colloid Interface Sci. 532, 375–386. https://doi.org/10.1016/J.JCIS.2018.07.130.

Choi, W., Hong, S., Jeong, Y., Cho, Y., Shin, H.G., Park, J.H., Yi, Y., Im, S., 2021. Dynamic oscillation via negative differential resistance in type III junction organic/two-dimensional and oxide/two-dimensional transition metal dichalcogenide diodes. Adv. Funct. Mater. 31, 2009436. https://doi.org/10.1002/ADFM.202009436.

Chou, Y., Lin, Y., Lu, C., Liu, F., J.L.-J. of, 2021. Undefined: Controlled Hydrothermal Synthesis of BiOxCly/BiOmBrn/g-C3n4 Composites Exhibiting Visible-Light Photocatalytic Activity. Elsevier.

Deng, Z., Chen, D., Peng, B., Tang, F., 2008. From bulk metal Bi to two-dimensional well-crystallized BiOX (X = Cl, Br) micro- and nanostructures: synthesis and characterization. Cryst. Growth Des. 8, 2995–3003. https://doi.org/10.1021/cg800116m.

Dutta, V., Singh, P., Shandilya, P., Sharma, S., Raizada, P., Saini, A.K., Gupta, V.K., Hosseini-Bandegharaei, A., Agarwal, S., Rahmani-Sani, A., 2019. Review on Advances in Photocatalytic Water Disinfection Utilizing Graphene and Graphene Derivatives-Based Nanocomposites.

Etaiw, S.E.H., Marie, H., 2018. Ultrasonic synthesis of 1D-Zn (II) and La (III) supramolecular coordination polymers nanoparticles, fluorescence, sensing and photocatalytic property. J. Photochem. Photobiol. Chem. 364, 478–491.

Fenichel, P., Chevalier, N., Brucker-Davis, F., 2013. Bisphenol A: an endocrine and metabolic disruptor. Ann. Endocrinol. 74, 211–220. https://doi.org/10.1016/J.ANDO.2013.04.002.

Fu, J.Y., Chen, L.W., Dai, Y.M., Liu, F.Y., Huang, S.T., Chen, C.C., 2018. BiOmFn/BiOxIy/GO Nanocomposites: synthesis, characterization, and photocatalytic activity. Molecul. Catal. 455, 214–223. https://doi.org/10.1016/J.MCAT.2018.06.014.

Gao, P., Yang, Y., Yin, Z., Kang, F., Fan, W., Sheng, J., Feng, L., Liu, Y., Du, Z., Zhang, L., 2021. A critical review on bismuth oxyhalide based photocatalysis for pharmaceutical active compounds degradation: modifications, reactive sites, and challenges. J. Hazard Mater. 412, 125186. https://doi.org/10.1016/J.JHAZMAT.2021.125186.

Garg, S., Yadav, M., Chandra, A., Sapra, S., Gahlawat, S., Ingole, P.P., Pap, Z., Hernadi, K. %J.R.S.C., 2018a. Advances: Biofabricated BiOI with Enhanced Photocatalytic Activity under Visible Light Irradiation, vol. 8, pp. 29022–29030.

Garg, S., Yadav, M., Chandra, A., Gahlawat, S., Ingole, P.P., Pap, Z., Hernadi, K., 2018b. Plant leaf extracts as photocatalytic activity tailoring agents for BiOCl towards environmental remediation. Ecotoxicol. Environ. Saf. 165, 357–366. https://doi.org/10.1016/j.ecoenv.2018.09.024.

Garg, S., Yadav, M., Chandra, A., Sapra, S., Gahlawat, S., Ingole, P.P., Pap, Z., Hernadi, K., 2018c. Biofabricated BiOI with enhanced photocatalytic activity under visible light irradiation. RSC Adv. 8, 29022–29030. https://doi.org/10.1039/c8ra05661g.

Garg, S., Yadav, M., Chandra, A., Gahlawat, S., Ingole, P.P., Pap, Z., Hernadi, K., 2018d. %J E., Safety, Environmental: Plant Leaf Extracts as Photocatalytic Activity Tailoring Agents for BiOCl towards Environmental Remediation, vol. 165, pp. 357–366.

Garg, S., Yadav, M., Chandra, A., Hernadi, K., 2019. A review on BiOX (X= Cl, Br and I) nano-/microstructures for their photocatalytic applications. J. Nanosci. Nanotechnol. 19, 280–294. https://doi.org/10.1166/jnn.2019.15771.

Hao, P.-P., 2020. Determination of Bisphenol A in Barreled Drinking Water by a SPE–LC–MS Method, pp. 697–703. https://doi.org/10.1080/10934529.2020.1732764 https://doi.org/10.1080/10934529.2020.1732764. 55.

Huang, W.L., 2009. Electronic structures and optical properties of BiOX (X = F, Cl, Br, I) via DFT calculations. J. Comput. Chem. 30, 1882–1891. https://doi.org/10.1002/JCC.21191.

Huang, S.T., Jiang, Y.R., Chou, S.Y., Dai, Y.M., Chen, C.C., 2014. Synthesis, characterization, photocatalytic activity of visible-light-responsive photocatalysts BiOxCly/BiOmBrn by controlled hydrothermal method. J. Mol. Catal. Chem. 391, 105–120. https://doi.org/10.1016/J.MOLCATA.2014.04.020.

Jiang, Y.R., Chou, S.Y., Chang, J.L., Huang, S.T., Lin, H.P., Chen, C.C., 2015a. Hydrothermal synthesis of bismuth oxybromide–bismuth oxyiodide composites with high visible light photocatalytic performance for the degradation of CV and phenol. RSC Adv. 5, 30851–30860. https://doi.org/10.1039/C5RA01702E.

Jiang, Y.R., Lin, H.P., Chung, W.H., Dai, Y.M., Lin, W.Y., Chen, C.C., 2015b. Controlled hydrothermal synthesis of BiOxCly/BiOmIn composites exhibiting visible-light photocatalytic degradation of crystal violet. J. Hazard Mater. 283, 787–805. https://doi.org/10.1016/J.JHAZMAT.2014.10.025.

Jiang, Y.R., Lin, H.P., Chung, W.H., Dai, Y.M., Lin, W.Y., Chen, C.C., 2015c. Controlled hydrothermal synthesis of BiOxCly/BiOmIn composites exhibiting visible-light photocatalytic degradation of crystal violet. J. Hazard Mater. 283, 787–805. https://doi.org/10.1016/J.JHAZMAT.2014.10.025.

Jing, L., He, M., Xie, M., Song, Y., Wei, W., Xu, Y., Xu, H., Li, H., 2021. Realizing the synergistic effect of electronic modulation over graphitic carbon nitride for highly efficient photodegradation of bisphenol A and 2-mercaptobenzothiazole: mechanism, degradation pathway and density functional theory calculation. J. Colloid Interface Sci. 583, 113–127. https://doi.org/10.1016/J.JCIS.2020.08.124.

Lee, A., Wang, Y., science, C.C.-J. of colloid and interface, 2019. Undefined: Composite Photocatalyst, Tetragonal Lead Bismuth Oxyiodide/bismuth Oxyiodide/graphitic Carbon Nitride: Synthesis, Characterization, and Photocatalytic Activity. Elsevier.

Li, K.L., Lee, W.W., Lu, C.S., Dai, Y.M., Chou, S.Y., Chen, H.L., Lin, H.P., Chen, C.C., 2014. Synthesis of BiOBr, Bi3O4Br, and Bi12O17Br2 by controlled hydrothermal method and their photocatalytic properties. J. Taiwan Inst. Chem. Eng. 45, 2688–2697. https://doi.org/10.1016/J.JTICE.2014.04.001.

Li, L., Niu, C.G., Guo, H., Wang, J., Ruan, M., Zhang, L., Liang, C., Liu, H.Y., Yang, Y.Y., 2020. Efficient degradation of Levofloxacin with magnetically separable ZnFe2O4/NCDs/Ag2CO3 Z-scheme heterojunction photocatalyst: vis-NIR light response ability and mechanism insight. Chem. Eng. J. 383, 123192. https://doi.org/10.1016/J.CEJ.2019.123192.

Li, K., Ma, S., Xu, S., Fu, H., Li, Z., Li, Y., Liu, S., Du, J., 2021a. The mechanism changes during bisphenol A degradation in three iron functionalized biochar/peroxymonosulfate systems: the crucial roles of iron contents and graphitized carbon layers. J. Hazard Mater. 404, 124145. https://doi.org/10.1016/J.JHAZMAT.2020.124145.

Li, Y., Liu, T., Cheng, Z., Peng, Y., Yang, S., Zhang, Y., 2021b. Facile synthesis of high crystallinity and oxygen vacancies rich bismuth oxybromide upconversion nanosheets by air-annealing for UV–Vis–NIR broad spectrum driven Bisphenol A degradation. Chem. Eng. J. 421, 127868. https://doi.org/10.1016/J. CEJ.2020.127868.

Li, J., Chen, J., Fang, H., Guo, X., Rui, Z., 2021c. Plasmonic metal bridge leading type III heterojunctions to robust type B photothermocatalysts. Ind. Eng. Chem. Res. 60, 8420–8429. https://doi.org/10.1021/acs.iecr.1c01198.

Liu, H., Yang, C., Huang, J., Chen, J., Zhong, J., Li, J., 2020. Ionic liquid-assisted hydrothermal preparation of BiOI/BiOCl heterojunctions with enhanced separation efficiency of photo-generated charge pairs and photocatalytic performance. Inorg. Chem. Commun. 113, 107806. https://doi.org/10.1016/J.INOCHE.2020.107806.

Lofrano, G., Carotenuto, M., Libralato, G., Domingos, R.F., Markus, A., Dini, L., Gautam, R.K., Baldantoni, D., Rossi, M., Sharma, S.K., Chattopadhyaya, M.C., Giugni, M., Meric, S., 2016. Polymer Functionalized Nanocomposites for Metals Removal from Water and Wastewater: an Overview.

Lucida, H., Febriyenti, R., Letter, L.R.-D.P., 2016. Undefined: Preparation of Quercetin Nanocrystals by Planetary Ball Mill to Increase the Solubility and the Dissolution Profile. researchgate.net.

Ma, F.Q., Yao, J.W., Zhang, Y.F., Wei, Y., 2017. Unique band structure enhanced visible light photocatalytic activity of phosphorus-doped BiOI hierarchical microspheres. RSC Adv. 7, 36288–36296. https://doi.org/10.1039/C7RA06261C.

Noorjahan, M., Kumari, V.D., Subrahmanyam, M., Boule, P., 2004. A novel and efficient photocatalyst: TiO2-HZSM-5 combinate thin film. Appl. Catal. B Environ. 47, 209–213. https://doi.org/10.1016/j.apcatb.2003.08.004.

Réti, B., Mogyorósi, K., Dombi, A., Hernádi, K., 2014. Substrate dependent photocatalytic performance of TiO2/MWCNT photocatalysts. Appl. Catal. Gen. 469, 153–158. https://doi.org/10.1016/j.apcata.2013.10.001.

Rochester, J.R., 2013a. Bisphenol A and human health: a review of the literature. Reprod. Toxicol. 42, 132–155. https://doi.org/10.1016/J.REPROTOX.2013.08.008.

Rochester, J.R., 2013b. Bisphenol A and human health: a review of the literature. Reprod. Toxicol. 42, 132–155. https://doi.org/10.1016/J.REPROTOX.2013.08.008.

Sajid, M.M., Khan, S.B., Shad, N.A., Amin, N., Zhang, Z., 2018. Visible light assisted photocatalytic degradation of crystal violet dye and electrochemical detection of ascorbic acid using a BiVO 4/FeVO 4 heterojunction composite. RSC Adv. 8, 23489–23498. https://doi.org/10.1039/C8RA03890B.

Salaeh, S., Juretic Perisic, D., Biosic, M., Kusic, H., Babic, S., Lavrencic Stangar, U., Dionysiou, D.D., Loncaric Bozic, A., 2016. Diclofenac removal by simulated solar assisted photocatalysis using TiO2-based zeolite catalyst; mechanisms, pathways and environmental aspects. Chem. Eng. J. 304, 289–302. https://doi.org/10.1016/j. cej.2016.06.083.

Sekar, K., Kassam, A., Bai, Y., Coulson, B., Li, W., Douthwaite, R.E., Sasaki, K., Lee, A.F., 2021. Hierarchical bismuth vanadate/re duce d graphene oxide composite photocatalyst for hydrogen evolution and bisphenol A degradation. Appl. Mater. Today 22, 100963. https://doi.org/10.1016/j.apmt.2021.100963.

Sharma, K., Dutta, V., Sharma, S., Raizada, P., Hosseini-Bandegharaei, A., Thakur, P., Singh, P., 2019. %J J. Of I., Chemistry, E.: Recent Advances in Enhanced Photocatalytic Activity of Bismuth Oxyhalides for Efficient Photocatalysis of Organic Pollutants in Water: A Review.

Siao, C., Chen, H., Chen, L., J.C.-J. of colloid and, 2018. Undefined: Controlled Hydrothermal Synthesis of Bismuth Oxychloride/bismuth Oxybromide/bismuth Oxyiodide Composites Exhibiting Visible-Light Photocatalytic. Elsevier.

Siao, C., Lee, W., Dai, Y., W.C.-J. of colloid and, 2019. Undefined: BiOxCly/BiOmBrn/ BiOpIq/GO Quaternary Composites: Syntheses and Application of Visible-Light-Driven Photocatalytic Activities. Elsevier.

Singh, S., Sharma, R., Khanuja, M., 2018. %J K.J. of C.E.: a review and recent developments on strategies to improve the photocatalytic elimination of organic dye pollutants by BiOX (X= Cl. Br, I, F) nanostructures 35, 1955–1968.

Tang, Z.-K., Yin, W.-J., Zhang, L., Wen, B., Zhang, D.-Y., Liu, L.-M., Lau, W.-M., 2016. Spatial separation of photo-generated electron-hole pairs in BiOBr/BiOI bilayer to facilitate water splitting. Sci. Rep. 6, 1–9. https://doi.org/10.1038/srep32764.

Tyagi, H., Chawla, H., Bhandari, H., Garg, S., 2021. Recent-enhancements in visible-light photocatalytic degradation of organochlorines pesticides: a review. Mater. Today Proc. https://doi.org/10.1016/j.matpr.2020.12.1036.

Wang, J., Huang, Y., Guo, J., Zhang, J., Wei, X., Ma, F., 2020. Optoelectronic response and interfacial properties of BiOI/BiOX (X=F, Cl, Br) heterostructures based on DFT investigation. J. Solid State Chem. 284, 121181. https://doi.org/10.1016/J. JSSC.2020.121181.

Wu, S., Xiong, J., Sun, J., Hood, D., Z, Zeng, W., Yang, Z., Gu, L., Zhang, X., Yang, S.-Z., 2017. Hydroxyl-Dependent evolution of oxygen vacancies enables the regeneration of BiOCl photocatalyst. ACS Appl. Mater. Interfaces 9, 16620–16626. https://doi. org/10.1021/acsami.7b01701.

Wu, L., Zhang, Q., Li, Z., Liu, X., 2020. Mechanochemical syntheses of a series of bismuth oxyhalide composites to progressively enhance the visible-light responsive activities for the degradation of bisphenol-A. Mater. Sci. Semicond. Process. 105, 104733. https://doi.org/10.1016/J.MSSP.2019.104733.

Xiao, X., Zhang, W.-D., 2010. Facile synthesis of nanostructured BiOI microspheres with high visible light-induced photocatalytic activity. J. Mater. Chem. 20, 5866–5870. https://doi.org/10.1039/C0JM00333F.

Xiao, X., Xing, C., He, G., Zuo, X., Nan, J., Wang, L., 2014. Solvothermal synthesis of novel hierarchical Bi4O5I2 nanoflakes with highly visible light photocatalytic performance for the degradation of 4-tert-butylphenol. Appl. Catal. B Environ. 148–149, 154–163. https://doi.org/10.1016/J.APCATB.2013.10.055.

Yadav, M., Garg, S., Chandra, A., Hernadi, K., 2019a. Immobilization of green BiOX (X= Cl, Br and I) photocatalysts on ceramic fibers for enhanced photocatalytic degradation of recalcitrant organic pollutants and efficient regeneration process. Ceram. Int. 45, 17715–17722. https://doi.org/10.1016/j.ceramint.2019.05.340.

Yadav, M., Garg, S., Chandra, A., Hernadi, K., 2019b. %J J. Of Colloid, Science, Interface: Fabrication of Leaf Extract Mediated Bismuth Oxybromide/oxyiodide (BiOBrxI1− x) Photocatalysts with Tunable Band Gap and Enhanced Optical Absorption for Degradation of Organic Pollutants, vol. 555, pp. 304–314.

Yadav, M., Garg, S., Chandra, A., Hernadi, K., 2019c. Quercetin-sensitized BiOF nanostructures: an investigation on photoinduced charge transfer and regeneration process for degradation of organic pollutants. J. Photochem. Photobiol. Chem. 383, 112014. https://doi.org/10.1016/J.JPHOTOCHEM.2019.112014.

Yadav, M., Garg, S., Chandra, A., Jyoti, Ingole, P.P., Bardos, E., Hernadi, K., 2021. Quercetin-mediated 3-D hierarchical BiOI-Q and BiOI-Q-Ag nanostructures with enhanced photodegradation efficiency. J. Alloys Compd. 856, 156812. https://doi. org/10.1016/j.jallcom.2020.156812.

Yu, Y., Chen, G., Wang, X., Jia, D., Tang, P., Lv, C., 2015a. A facile approach to construct BiOI/Bi5O7I composites with heterostructures: efficient charge separation and enhanced photocatalytic activity. RSC Adv. 5, 74174–74179. https://doi.org/ 10.1039/C5RA13755A.

Yu, Y., Chen, G., Wang, X., Jia, D., Tang, P., Lv, C., 2015b. A facile approach to construct BiOI/Bi5O7I composites with heterostructures: efficient charge separation and enhanced photocatalytic activity. RSC Adv. 5, 74174–74179. https://doi.org/ 10.1039/C5RA13755A.

Zhang, L., Tang, Z.-K., Lau, W.-M., Yin, W.-J., Hu, S.-X., Liu, L.-M., 2017. Tuning band gaps and optical absorption of BiOCl through doping and strain: insight form DFT calculations. Phys. Chem. Chem. Phys. 19, 20968–20973. https://doi.org/10.1039/ C7CP03276E.

Zhang, S., Zhang, J., Sun, J., Tang, Z., 2020. Capillary microphotoreactor packed with TiO2-coated glass beads: an efficient tool for photocatalytic reaction. Chem. Eng. Proc. Process Intensif. 147, 107746. https://doi.org/10.1016/j.cep.2019.107746.

Zhao, Y., Zhou, S., Zhao, J., Du, Y., Dou, S.X., 2020. Control of photocarrier separation and recombination at bismuth oxyhalide interface for nitrogen fixation. J. Phys. Chem. Lett. 9304–9312. https://doi.org/10.1021/ACS.JPCLETT.0C02480.

Zhou, S., Shi, T., Chen, Z., Kilin, D.S., Shui, L., Jin, M., Yi, Z., Yuan, M., Li, N., Yang, X., Meng, Q., Wang, X., Zhou, G., 2019. First-principles study of optoelectronic properties of the noble metal (Ag and Pd) doped BiOX (X = F, Cl, Br, and I) photocatalytic system. Catalysts 9, 198. https://doi.org/10.3390/CATAL9020198.